Signal Processing for TDM MIMO FMCW Millimeter-Wave Radar Sensors

XINRONG LI[1], **(Senior Member, IEEE), XIAODONG WANG**[1],
QING YANG[2], **(Senior Member, IEEE), AND SONG FU**[2], **(Senior Member, IEEE)**
[1]Department of Electrical Engineering, University of North Texas (UNT), Denton, TX 76203, USA
[2]Department of Computer Science and Engineering, University of North Texas (UNT), Denton, TX 76203, USA

Corresponding author: Xinrong Li (xinrong.li@unt.edu)

ABSTRACT In this tutorial paper, we systematically present the fundamental operating principles and analytical details of the discrete Fourier transform based signal processing techniques for the TDM MIMO FMCW millimeter-wave (mmWave) automotive radars. The mmWave radars provide a key sensing capability to support safety features of the conventional and autonomous vehicles. Automotive radar sensors are used to detect presence and location of the objects of interest to derive comprehensive and accurate knowledge of road conditions and surrounding environments. Automotive radars are subjected to an increasing demand to provide high-resolution measurements in the range-Doppler-azimuth-elevation domains. Therefore, the current state-of-the-art automotive radars commonly employ MIMO technologies, resulting in a large block of multidimensional data to process in real time through a long chain of signal processing algorithms. Detailed coverage on the fundamental radar signal processing techniques are scattered in a large body of literature for classical radar systems. Currently, there is no tutorial available that covers the technical details of the latest TDM MIMO FMCW radar technology, making it extremely hard for new researchers in the field of automotive mmWave radars. This paper contains sufficient technical details to serve as a tutorial. It can help lay a solid analytical foundation to facilitate exploration and development of advanced radar signal processing techniques for automotive applications. The algorithmic details and analytical results presented in this paper can be readily applied to both real-time implementation and post-processing. Simulation and experimental results are presented in this paper to validate analytical derivations and to demonstrate the capabilities of the TDM MIMO radar sensor in practical implementations.

INDEX TERMS AOA, automotive, Doppler, ranging, MIMO, mmWave.

I. INTRODUCTION

Automotive radar sensors are becoming a key component of autonomous vehicles and the advanced driver assistant system (ADAS) of conventional vehicles. Safety features that can be supported by such sensors include automatic emergency braking (AEB), autonomous emergency steering (AES), adaptive cruise control (ACC), forward collision warning (FCW), and lane change assistance (LCA), among many others [1]–[8]. Automotive radar sensors can be used to detect presence and location of the objects of interest by estimating their range, velocity, and angle. The objectives of automotive radar sensors are to derive comprehensive and accurate knowledge of road conditions and surrounding environments to effectively protect the safety of vehicle occu-

pants and vulnerable road users. Radar sensors are insensitive to lighting variations and weather conditions, can provide accurate measurements of range and velocity, and can be packaged behind optically nontransparent fascia. Therefore, radar sensors can fit nicely in the automotive safety sensor suite to complement the capabilities of other types of sensors such as camera and lidar [5]–[7].

Recently, extensive research and development efforts have been focused on millimeter wave (mmWave) radar technologies for automotive and industrial applications. The current state-of-the-art automotive radars employ linear frequency-modulated continuous-wave (FMCW) signals, the mmWave frequency band at 76 - 81 GHz, and multiple-input multiple-output (MIMO) technologies [5]. The mmWave radars transmit signals with a wavelength in the millimeter range. Thus, it is possible to reduce the size of components, antennas, and the system, while providing millimeter-level

The associate editor coordinating the review of this manuscript and approving it for publication was Hassan Omar.

accuracy in movement detection. MIMO radars with colocated transmit and receive antennas can provide large virtual aperture to improve angle estimation performance. MIMO radars achieve waveform orthogonality by using a multiplexing technique such as time-division multiplexing (TDM), frequency-division multiplexing (FDM), and code-division multiplexing (CDM) [6]–[11]. TDM is often used in automotive radars for its simplicity and low cost in practical implementations [11]. Significant advances in mmWave semiconductor devices and RF CMOS technologies have enabled high-level radar-on-chip integrations [3]–[8], [12], [13]. Single-chip radar solutions are now available from several semiconductor manufacturers such as Texas Instruments [3] and NXP [4].

Signal processing has always been a critical component of radar technology [14], [15]. The uniqueness of automotive radar applications require formulation and derivation of new signal processing approaches beyond the classical radar concepts [5]. As a result, in the past few years, there has been a steady increase in research and development efforts focused on various aspects of automotive radar signal processing. Several review papers exist in the recent literature that cover briefly many signal processing aspects of automotive radars [5]–[7]. However, currently there is no comprehensive tutorial paper available in the literature that covers the technical details of the latest TDM MIMO FMCW radar technology. A number of brief tutorials are available from the manufacturers of the mmWave radar devices in the forms of whitepapers and application notes such as [12], [16], [18]. These tutorials only contain limited introductory materials and selected results without sufficient analytical details or in-depth analysis. On the other hand, detailed coverage on the fundamental radar signal processing techniques are scattered in a large body of literature for classical radar technologies (see for example [14], [15] and a large number of references therein). Often times, significant efforts are required to generalize the classical techniques to the new automotive applications, making it extremely hard for new researchers and practitioners in the field.

Automotive radars are subjected to an increasing demand to provide high-resolution multidimensional measurements in the range-Doppler-azimuth-elevation domains [5]–[7]. Therefore, state-of-the-art automotive radars commonly employ the MIMO technologies. As compared to the conventional radars, MIMO radars result in an even larger block of multidimensional data that need to be processed through a long chain of signal processing algorithms [5]–[7], [12], [13]. The goal of this tutorial paper is to systematically present the fundamental operating principles and analytical details of the discrete Fourier transform (DFT) based signal processing techniques for the latest TDM MIMO FMCW mmWave radars. This paper contains sufficient technical details to serve as a tutorial. Thus, this paper fills a gap in the current literature. It can help lay a solid analytical foundation to facilitate exploration and development of advanced radar signal processing techniques for automotive applications. Since

the derivations and analysis are based on the fundamental DFT theories, the algorithmic details and analytical results presented in this paper can be readily applied to both real-time implementation and post-processing. Simulation and experimental results are also presented to validate analytical derivations and to demonstrate the capabilities of the TDM MIMO radar sensors.

The rest of the paper is organized as follows. The signal and system models of the FMCW mmWave radars are presented in Section II. Then, range processing, Doppler processing, and angle processing are discussed in details in the next three sections. The state-of-the-art TDM MIMO radar technique is presented in Section VI. A brief description of radar signal processing flow is presented in Section VII. Some simulation and experimental results are presented in Sections VIII and IX, respectively, to validate analytical derivations and to demonstrate the capabilities of the TDM MIMO radar. A number of related works are reviewed in Section X. Finally, the paper is closed with a summary and conclusions in Section XI.

II. SIGNAL AND SYSTEM MODELS

A radar system transmits a signal $x_T(t)$ from its transmitter antenna (Tx) as shown in Fig. 1. When the signal strikes an object, part of the signal energy (i.e., radar returns or echoes) is reflected back to the radar receiver antenna (Rx), where it is received as the signal $x_R(t)$. Radar system processes the received signal $x_R(t)$ to extract range, velocity, and angle as well as other target characteristics to detect, locate, track, and identify target objects [14], [15].
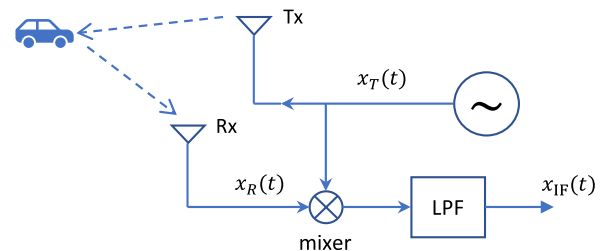

FIGURE 1. Block diagram of the radar system.

In this paper, we focus on a particular type of radar system that employs the linear FMCW signal. The linear FMCW signal can provide a large time-bandwidth product, which makes it possible to achieve high range resolution and signal-to-noise ratio (SNR) simultaneously [15]. The FMCW signal is characterized by the start frequency f_c, the bandwidth B, and the time duration T_c as shown in Fig. 2. The FMCW signal over the time duration T_c is known as a chirp. The frequency of the chirp signal increases linearly at the rate S over time. A sinusoidal FMCW signal can be represented as [16], [17]

$$x_T(t) = \cos(2\pi f_c t + \pi S t^2), \qquad (1)$$

while the instantaneous frequency is determined as

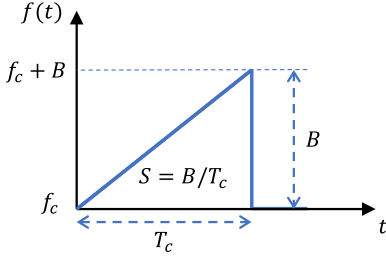$$f(t) = \frac{1}{2\pi}\frac{d}{dt}(2\pi f_c t + \pi S t^2) = f_c + St. \quad (2)$$

FIGURE 2. The FMCW chirp signal with the start frequency f_c, bandwidth B, slope S, and time duration T_c.

In operation, as shown in Fig. 1, the radar receiver mixes the received signal $x_R(t)$ with the transmitted signal $x_T(t)$ and low-pass filters the resulting signal to produce the intermediate frequency (IF) signal $x_{IF}(t)$. As the frequency of the FMCW signal $x_T(t)$ increases linearly over time, the instantaneous frequencies of $x_T(t)$ and $x_R(t)$, i.e., $f_T(t)$ and $f_R(t)$, are different at the time of mixing. The effect of low-pass filtering is to filter out the signal component of the frequency $f_T(t) + f_R(t)$ while allowing the signal component of the frequency $f_T(t) - f_R(t)$ to pass through. That is,

$$x_{IF}(t) = \text{LPF}\{x_T(t)x_R(t)\} = A\cos(2\pi f_{IF}t + \phi_{IF}), \quad (3)$$

where $f_{IF} = f_T(t) - f_R(t)$. As explained below, f_{IF} is not a function of time, and it remains a constant. The constant frequency difference f_{IF} is known as beat frequency [14]. As often used in RF applications, quadrature signals can be used at the receiver to reduce the requirement on high-speed sampling of the IF signal among other design considerations [17]. With a quadrature receiver, the received signal $x_R(t)$ is mixed with the in-phase and quadrature signals of $x_T(t)$, resulting in a complex exponential IF signal for further processing [17],

$$x_{IF}(t) = Ae^{j(2\pi f_{IF}t + \phi_{IF})}. \quad (4)$$

For an object at the range (i.e., distance) r from the radar, the transmitted signal is reflected back by the object, and it
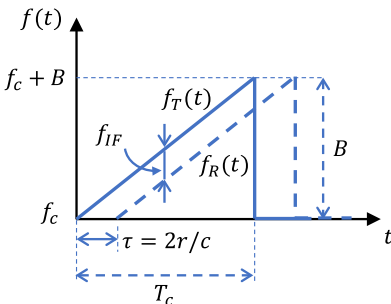

FIGURE 3. Derivation of the constant-frequency IF signal from the transmitted and received chirp signals.

arrives at the receiver antenna after a delay

$$\tau = 2r/c, \quad (5)$$

where c is the speed of light. As illustrated in Fig. 3, the IF signal frequency (i.e., beat frequency) remains a constant over the valid reception period when the transmitted and received chirp signals overlap in time. That is,

$$f_{IF} = f_T(t) - f_R(t) = S\tau, \quad (6)$$

where S is the slope of the linearly increasing frequency of the chirp signal as defined in (2). The phase of the IF signal in (4) can be determined at the start time instant of the IF signal when the reflected chirp signal arrives at the receiver antenna. Thus, given the chirp signal model in (1),

$$\phi_{IF} = 2\pi f_c \tau + \pi S\tau^2 \approx 2\pi f_c \tau, \quad (7)$$

since for typical mmWave radar systems, the start frequency f_c of the chirp signal is much larger than $S\tau/2$.

In summary, the IF signal corresponding to an object at the range r from the radar is a complex exponential signal

$$x_{IF}(t) = Ae^{j(2\pi f_{IF}t + \phi_{IF})}, \quad (8)$$

with the frequency and phase

$$f_{IF} = S\tau = 2Sr/c, \quad (9)$$

$$\phi_{IF} = 2\pi f_c \tau = 4\pi r/\lambda. \quad (10)$$

The parameter $\lambda = c/f_c$ is the wavelength of the chirp signal at the start frequency f_c. When multiple objects reflect the chirp signal back to radar, the received IF signal is a linear combination of multiple complex exponential signals, each of which has the frequency and phase corresponding to the range of each object. The rest of this paper is focused on the IF signal model in (8)-(10).

III. RANGE PROCESSING
A. RANGE-DFT
To perform further digital signal processing, the IF signal $x_{IF}(t)$ in (8) is sampled N_s times with the sampling frequency F_s. The resulting discrete-time complex exponential signal can be expressed as

$$x[n] = Ae^{j\phi_{IF}}e^{jn\omega_{IF}} \quad (11)$$

for $0 \le n < N_s$, where the discrete-time angular frequency

$$\omega_{IF} = 2\pi f_{IF}/F_s. \quad (12)$$

The Fourier transform of the finite-duration discrete-time signal $x[n]$ in (11) can be derived as [19]

$$X(\omega) = \mathcal{F}\{x[n]\} = \sum_{n=0}^{N_s-1} x[n]e^{-jn\omega}$$
$$= Ae^{j\phi_{IF}}P_{N_s}(\omega - \omega_{IF}), \quad (13)$$

where

$$P_N(\omega) = \sum_{n=0}^{N-1} e^{-jn\omega} = \frac{\sin(\omega N/2)}{\sin(\omega/2)}e^{-j\omega(N-1)/2}. \quad (14)$$

Apparently, $P_N(\omega)$ is the Fourier transform of the length-N square window function. Then, the discrete Fourier transform (DFT) of $x[n]$ can be expressed as

$$X[k] = \text{DFT}\{x[n]\} = X(\omega)|_{\omega=2\pi k/N_s}$$
$$= A e^{j\phi_{\text{IF}}} P_{N_s}\left(\frac{2\pi}{N_s}k - \omega_{\text{IF}}\right) \quad (15)$$

for $0 \le k < N_s$. According to the Fourier transform theory, the index k of the DFT $X[k]$ corresponds to the frequency $f_k = kF_s/N_s$. Therefore, based on the frequency-range relation in (9), the index axis of $X[k]$ can be converted to the range unit with

$$r_k = f_k \frac{c}{2S} = k\frac{cF_s}{2SN_s} = k\frac{c}{2S\tilde{T}_c} = k\frac{c}{2\tilde{B}} \quad (16)$$

for $0 \le k < N_s$. In (16), $\tilde{T}_c = N_s/F_s$ is the length of the sampled IF signal in time (i.e., ADC sampling window length) and $\tilde{B} = S\tilde{T}_c$ is the sweep bandwidth of chirp signal. Thus, r_k in (16) is referred to as range axis while $X[k]$ in (15) is referred to as range-DFT (or range-FFT). When plotted against the range axis, the magnitude spectrum $|X[k]|$ shows a sharp peak at the range corresponding to the object that reflects the chirp signal back to the radar receiver.

According to the Nyquist sampling theorem, the highest frequency component in the signal $x[n]$ should be at most $F_s/2$. However, when the quadrature receiver is used, for $0 < f_{\text{IF}} \le F_s/2$, the complex exponential IF signal in (8) has one-sided power spectrum over the positive frequency with no power on the negative frequency. For $F_s/2 < f_{\text{IF}} \le F_s$, the spectrum corresponding to f_{IF} appears at the negative frequency $f_{\text{IF}} - F_s$ as alias because f_{IF} is higher than the Nyquist sampling frequency $F_s/2$. Since f_{IF} is always positive due to the operating principles of the FMCW radar, the highest IF frequency that can be detected through the range-DFT in (15) can be extended to F_s by interpreting the spectrum over negative frequency between $-F_s/2$ and 0 as the spectrum over positive frequency between $F_s/2$ and F_s. Consequently, based on the frequency-range relation in (9), the range of the object that can be detected through the range-DFT is limited to

$$r < \frac{cF_s}{2S}, \quad (17)$$

and the range axis in (16) is valid for $0 \le k < N_s$. In practice, radar systems have a limited IF bandwidth. Thus, the maximum detectable range is determined by the maximum IF bandwidth B_{IF} if it is smaller than the sampling frequency F_s. That is, $r < cB_{\text{IF}}/(2S)$, if $B_{\text{IF}} < F_s$.

B. RANGE RESOLUTION

When multiple objects reflect the chirp signal back to radar, the time-domain received IF signal is a linear combination of individual IF signals that are resulted from each of the reflecting objects. Since the DFT is a linear transformation, the overall range spectrum of multiple objects is a linear combination of the spectra of the individual reflecting

objects. Consequently, the objects with different ranges can be detected from the peaks in the range spectrum.

According to the Fourier transform theory, the frequency resolution of the signal of length $\tilde{T}_c$ in time is given by $f_{\text{res}} = 1/\tilde{T}_c$ [19]. As a result, based on (9), the range resolution of the IF signal can be determined as [14], [15]

$$r_{\text{res}} = \frac{c}{2S}f_{\text{res}} = \frac{c}{2S\tilde{T}_c} = \frac{c}{2\tilde{B}}. \quad (18)$$

The sweep bandwidth $\tilde{B}$ is the same as in (16). Thus, with the range-DFT, it is possible to distinguish two objects that are separated by more than $c/(2\tilde{B})$ in range. In practice, a window function such as Hamming, Hanning, or Blackman window is applied to the time-domain signal $x[n]$ before performing DFT (i.e., FFT) to reduce sidelobes [19]. The use of a window function helps improve the accuracy of object detection. However, the use of window function also degrades range resolution. For example, with the Hamming or Hanning window, the range resolution doubles as compared to (18), i.e., $r_{\text{res}} = c/\tilde{B}$, because the width of the main lobe of the Hamming or Hanning window is twice as large as the rectangular window [19].

IV. DOPPLER PROCESSING
A. DOPPLER-DFT
To measure the velocity of an object, radar can transmit two chirp signals that are separated by T_c in time. If the velocity of the object is v, over the time duration of T_c, the object travels a distance of $\Delta r = vT_c$. Based on the IF signal model in (9) and (10), the differences in frequency and phase between the IF signals derived from the two chirps are

$$\Delta f = 2S\Delta r/c = 2SvT_c/c, \quad (19)$$
$$\Delta\phi = 4\pi\Delta r/\lambda = 4\pi vT_c/\lambda. \quad (20)$$

When the time T_c is small, Δf is negligible as compared to the frequency of the IF signal. However, the phase difference can be detected even when the movement Δr is in the order of millimeter, i.e., in the order of the wavelength λ of the mmWave chirp signals.
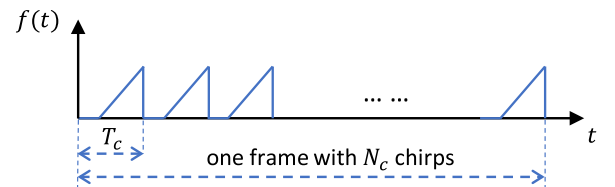

FIGURE 4. A frame of N_c chirps equally spaced by T_c in time.

In practice, as shown in Fig. 4, radar transmits a set of N_c chirps equally spaced by T_c in time. The set of chirps is known as a chirp frame and T_c is the chirp cycle time [16]. Define $x_m[n]$, $0 \le n < N_s$, to be the sampled IF signal derived from the mth chirp. Then, the range-DFT of the mth chirp becomes

$$X_m[k] = |X_m[k]|e^{j\phi_m[k]} = \text{DFT}\{x_m[n]\} \quad (21)$$

for $0 \le m < N_c$ and $0 \le k < N_s$, where $|X_m[k]|$ and $\phi_m[k]$ are the magnitude and phase of $X_m[k]$, respectively.

For one single moving object, since Δf in (19) is negligible when T_c is small, we can observe from (15) that along the m-axis for a given k, the angular frequency ω_{IF} and the magnitude of $X_m[k]$ remain constant. However, based on (20), the phase of $X_m[k]$ changes linearly due to the equal spacing of the chirps in the frame. Thus, we can derive that

$$|X_m[k]| = |X_0[k]|, \tag{22}$$

$$\phi_m[k] = \phi_0[k] + \frac{4\pi v T_c}{\lambda} m, \tag{23}$$

for $0 \le m < N_c$ and $0 \le k < N_s$. Furthermore, define

$$y_k[m] = X_m[k] = X_0[k] e^{jm\omega_v} \tag{24}$$

for $0 \le m < N_c$ and $0 \le k < N_s$, where

$$\omega_v = 4\pi v T_c / \lambda. \tag{25}$$

Then, we can observe that for a given k, $y_k[m]$ is a finite-duration discrete-time complex exponential signal with the discrete-time angular frequency ω_v defined in (25).

Similar to the discussion for the range-DFT, a second DFT can now be applied to the finite-duration discrete-time sequence $y_k[m]$ to extract the object velocity. It is often referred to as Doppler-DFT (or Doppler-FFT),

$$Y_k[l] = \text{DFT}\{y_k[m]\} = X_0[k] P_{N_c}\left(\frac{2\pi}{N_c} l - \omega_v\right) \tag{26}$$

for $0 \le l < N_c$ and $0 \le k < N_s$. The function $P_N(\omega)$ is defined in (14).

According to the Fourier transform theory, the DFT $Y_k[l]$ is a periodic sequence with a period of N_c for $-\infty < l < \infty$. The index l corresponds to the discrete-time angular frequency $\omega_l = 2\pi l / N_c$. For unambiguous measurement of the velocity v, the angular frequency is limited to the range $-\pi \le \omega < \pi$, or equivalently, $-N_c/2 \le l < N_c/2$, assuming N_c is an even number as in the case where the FFT is used. Therefore, based on the angular frequency-velocity relation in (25), the index axis of $Y_k[l]$ can be converted to the velocity unit with

$$v_l = \omega_l \frac{\lambda}{4\pi T_c} = l \frac{\lambda}{2N_c T_c} = l \frac{\lambda}{2T_F} \tag{27}$$

for $-N_c/2 \le l < N_c/2$. The parameter $T_F = N_c T_c$ is the frame duration in time, and it is traditionally known as the time on target (TOT) [5], [14].

The Doppler-DFT spectrum $Y_k[l]$ for a given k can now be plotted against the velocity axis. Thus, the velocity that is detectable through the Doppler-DFT is limited to

$$-\frac{\lambda}{4T_c} \le v < \frac{\lambda}{4T_c}. \tag{28}$$

A positive velocity indicates the object moving away from the radar and a negative velocity indicates the object moving towards the radar. The Doppler-DFT spectrum $Y_k[l]$ given in (26) is often visualized with the 2D heatmap or 3D mesh plots. The object reflecting the chirp signals back to the radar

can be distinguished with a sharp peak in the range-velocity (i.e., range-Doppler) spectrum at the coordinate corresponding to the object's range and velocity values.

B. VELOCITY RESOLUTION
When multiple objects reflect the chirp signals back to the radar, the time-domain received IF signal is a linear combination of individual IF signals that are resulted from each of the reflecting objects. Since the DFT is a linear transformation, the overall range-velocity spectrum of multiple objects is a linear combination of the spectra of the individual reflecting objects. Consequently, the objects with different range and/or velocity can be detected from the peaks in the range-velocity spectrum.

The angular frequency resolution of a discrete-time signal of length N_c is given by $\omega_{\text{res}} = 2\pi/N_c$ [19]. Thus, based on (25), the velocity resolution can be determined as

$$v_{\text{res}} = \frac{\lambda}{4\pi T_c} \omega_{\text{res}} = \frac{\lambda}{2N_c T_c} = \frac{\lambda}{2T_F}, \tag{29}$$

where the frame duration T_F is the same as in (27). With the Doppler-DFT, it is possible to distinguish two objects at the same range but with a velocity difference that is larger than $\lambda/(2T_F)$. In addition, similar to our earlier discussion for the range processing, when the Hamming or Hanning window is applied before the Doppler-DFT to reduce the sidelobes, the velocity resolution degrades to $v_{\text{res}} = \lambda/T_F$.

V. ANGLE PROCESSING
A. ANGLE-DFT
The arriving direction of the radar chirp signal reflected by an object can be estimated using a receiver antenna array. Fig. 5 illustrates the direction estimation scenario using a uniform linear array of four equally spaced receiver antennas. Assume the object is in the far field of the radar system. That is, assume the range between the object and the radar is much larger than the dimension (or, more accurately, the aperture) of the antenna array. Then, the signals arriving at the receiver antennas as well as the signal reaching the object from the transmitter antenna can all be assumed to be in parallel. As shown in Fig. 5, define the angle of arrival (AOA) or direction of arrival (DOA) θ of the received signal relative to the antenna array boresight direction that is perpendicular to the axis of the linear receiver antenna array.

As illustrated in Fig. 5, due to the spacing between receiver antennas, the relative delay experienced by the signals arriving at two adjacent receiver antennas can be determined as

$$\Delta \tau = d \sin(\theta)/c. \tag{30}$$

In this equation, d is the antenna spacing, θ is the AOA of the received radar signal, and c is the speed of light. Then, based on the IF signal model in (9) and (10), the differences in frequency and phase between the IF signals received at two adjacent receiver antennas are

$$\Delta f = S \Delta \tau = S d \sin(\theta)/c, \tag{31}$$
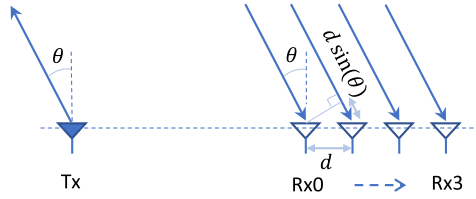
FIGURE 5. Angle estimation with a uniform linear array of four receiver antennas.

$$\Delta\phi = 2\pi f_c \Delta\tau = 2\pi d \sin(\theta)/\lambda. \quad (32)$$

The parameter $\lambda = c/f_c$ is the wavelength of the chirp signal at the start frequency f_c. Similar to the discussion for the Doppler processing, when d is small relative to the range r of the reflecting object, the frequency difference Δf in (31) is negligible as compared to the IF signal frequency. However, the phase difference $\Delta\phi$ in (32) is detectable as discussed in detail in the following.

With a uniform linear antenna array at the radar receiver, assume a set of N_R antennas are placed on a straight line with a uniform spacing d as shown in Fig. 5. For each of the chirp signal transmitted by the radar, the radar receiver derives one IF signal from each of the N_R receiver antennas. Denote the sampled IF signal from the ith receiver antenna as $x^{(i)}[n]$ for $0 \le i < N_R$ and $0 \le n < N_s$. Then, the range-DFT of the sampled IF signal derived from the ith receiver antenna can be represented as

$$X^{(i)}[k] = |X^{(i)}[k]|e^{j\phi^{(i)}[k]} = \mathrm{DFT}\{x^{(i)}[n]\} \quad (33)$$

for $0 \le i < N_R$ and $0 \le k < N_s$. $|X^{(i)}[k]|$ and $\phi^{(i)}[k]$ are the magnitude and phase of $X^{(i)}[k]$, respectively.

For one single object reflecting the chirp signal back to the radar receiver, since Δf in (31) is negligible when the object is in the far field, we can observe from (15) that along the i-axis for a given k, the angular frequency ω_{IF} and thus the magnitude of $X^{(i)}[k]$ remain constant. However, based on (32), the phase of $X^{(i)}[k]$ changes linearly due to the equal spacing of the receiver antennas in the uniform linear array. Thus, we can derive that

$$|X^{(i)}[k]| = |X^{(0)}[k]|, \quad (34)$$

$$\phi^{(i)}[k] = \phi^{(0)}[k] + \frac{2\pi d \sin(\theta)}{\lambda}i, \quad (35)$$

for $0 \le i < N_R$ and $0 \le k < N_s$, which leads to

$$X^{(i)}[k] = X^{(0)}[k]e^{ji\omega_\theta} \quad (36)$$

where

$$\omega_\theta = 2\pi d \sin(\theta)/\lambda. \quad (37)$$

Based on (26) and (36), we can also derive that the Doppler-DFT derived for the ith receiver antenna

$$Y_k^{(i)}[l] = X_0^{(i)}[k]P_{N_c}(\frac{2\pi}{N_c}l - \omega_v)$$
$$= X_0^{(0)}[k]P_{N_c}(\frac{2\pi}{N_c}l - \omega_v)e^{ji\omega_\theta} \quad (38)$$

for $0 \le k < N_s$, $0 \le l < N_c$, and $0 \le i < N_R$. $X_m^{(i)}[k]$ is the range-DFT of the mth chirp at the ith receiver antenna. Furthermore, define

$$z_{k,l}[i] = Y_k^{(i)}[l] \quad (39)$$

for $0 \le k < N_s$, $0 \le l < N_c$, and $0 \le i < N_R$. Then, we can observe that for the given values of k and l, $z_{k,l}[i]$ is a finite-duration discrete-time complex exponential signal with the discrete-time angular frequency ω_θ defined in (37).

Similar to the discussions for the range-DFT and Doppler-DFT, a third DFT can now be applied to the finite-duration discrete-time sequence $z_{k,l}[i]$ to extract the AOA. The third DFT is referred to as angle-DFT (or angle-FFT),

$$Z_{k,l}[\eta] = \mathrm{DFT}\{z_{k,l}[i]\}$$
$$= X_0^{(0)}[k]P_{N_c}(\frac{2\pi}{N_c}l - \omega_v)P_{N_R}(\frac{2\pi}{N_R}\eta - \omega_\theta) \quad (40)$$

for $0 \le \eta < N_R$, $0 \le k < N_s$, and $0 \le l < N_c$. The function $P_N(\omega)$ is defined in (14).

In practical implementations, the number of receiver antennas in the uniform linear array is typically small, resulting in a sparse-looking angle-DFT spectrum that is difficult to visualize and interpret. To address this issue, $z_{k,l}[i]$ is often padded with $N - N_R$ zeros at the end of the sequence to achieve a better display of the spectrum $Z_{k,l}[\eta]$ by using a much longer N-point DFT. According to the Fourier transform theory, with zero padding, the DFT $Z_{k,l}[\eta]$ is a periodic sequence with a period of N for $-\infty < \eta < \infty$, and the index η corresponds to the discrete-time angular frequency $\omega_\eta = 2\pi\eta/N$. For unambiguous measurement of the angle θ, the angular frequency is limited to the range $-\pi \le \omega < \pi$, or equivalently, $-N/2 \le \eta < N/2$, assuming N is an even number as in the case where FFT is used. Therefore, based on the angular frequency-angle relation in (37), the index axis of $Z_{k,l}[\eta]$ can be converted to the angle unit with

$$\theta_\eta = \sin^{-1}(\omega_\eta\frac{\lambda}{2\pi d}) = \sin^{-1}(\eta\frac{\lambda}{Nd}) \quad (41)$$

for $-N/2 \le \eta < N/2$. Thus, the angular field of view (FOV) of the linear antenna array can be determined as

$$-\sin^{-1}(\frac{\lambda}{2d}) \le \theta < \sin^{-1}(\frac{\lambda}{2d}). \quad (42)$$

When the receiver antenna spacing $d = \lambda/2$, the FOV is the largest, that is, $-90° \le \theta < 90°$.

B. ANGULAR RESOLUTION

When multiple objects reflect the chirp signals back to the radar, the time-domain received IF signal is a linear combination of individual IF signals that are resulted from each of the reflecting objects. Since DFT is a linear transformation, the angle-DFT spectrum is a linear combination of the spectra of individual reflecting objects. Consequently, the objects with different range, velocity, and/or angle can be clearly detected from the peaks in the 3D range-velocity-angle spectrum.

With zero padding, the angular frequency resolution of the DFT $Z_{k,l}[\eta]$ is still determined by N_R, that is, $\omega_{\mathrm{res}} = 2\pi/N_R$,

since zero padding does not improve the frequency resolution of DFT [19]. Because of the nonlinear relation between ω_θ and θ in (37), it is more complicated to derive the angular resolution than the velocity resolution in (29). To derive the angular resolution, we define

$$\omega_{\theta_1} = 2\pi d \sin(\theta_1)/\lambda,$$
$$\omega_{\theta_2} = 2\pi d \sin(\theta_1 + \Delta\theta)/\lambda.$$

Then, it is straightforward to determine that

$$\omega_{\theta_2} - \omega_{\theta_1} = \frac{4\pi d}{\lambda}\cos(\bar{\theta})\sin(\frac{\Delta\theta}{2}),$$

where $\bar{\theta} = \theta_1 + \Delta\theta/2$. By setting $|\omega_{\theta_2} - \omega_{\theta_1}| = \omega_{\mathrm{res}} = 2\pi/N_R$, we can derive that

$$\theta_{\mathrm{res}} = |\Delta\theta| = 2\sin^{-1}(\frac{\lambda}{2N_R d \cos(\bar{\theta})}). \qquad (43)$$

Therefore, with the angle-DFT, it is possible to distinguish two objects at the same range, with the same velocity, but with an angle difference that is larger than the θ_{res} given in (43). In addition, similar to our earlier discussions for range processing, when the Hamming or Hanning window is applied before the angle-DFT to reduce sidelobes, the angular resolution degrades.

It is important to note that the angular resolution in (43) depends on the value of $\bar{\theta}$, which is the mid-point between the two angles of interest. The angular resolution θ_{res} is the smallest when $\bar{\theta} = 0$, and it increases as $\bar{\theta}$ moves towards $\pm 90°$. The small-angle approximation is often used to simplify the angular resolution formula in (43). That is, when $\Delta\theta/2$ is small and measured in radians, $\sin(\Delta\theta/2) \approx \Delta\theta/2$, which can be used to derive that

$$\theta_{\mathrm{res}} = |\Delta\theta| = \frac{\lambda}{N_R d \cos(\bar{\theta})}. \qquad (44)$$

The angular resolution of linear antenna array is usually quoted for the boresight view (i.e., $\bar{\theta} = 0$) and the antenna spacing of $d = \lambda/2$, which leads to the angular resolution of

$$\theta_{\mathrm{res}} = 2/N_R \qquad (45)$$

in the unit of radians. For example, when the number of receiver antennas $N_R = 4$, the angular resolution of the linear receiver antenna array can be determined as $\theta_{\mathrm{res}} = 29°$.

VI. TDM MIMO RADAR FOR IMPROVED ANGULAR RESOLUTION

A. TDM MIMO RADAR

As shown in (43) and (44), the angular resolution of the uniform linear array directly depends on the number of receiver antennas. Increasing the number of receiver antennas can improve the angular resolution of the radar. However, each additional receiver antenna requires separate receiver processing chain on the device, which will increase the complexity and the cost of the radar receiver. In contrast, MIMO technology provides a cost-effective way to improve the angular resolution of radars [5], [12].
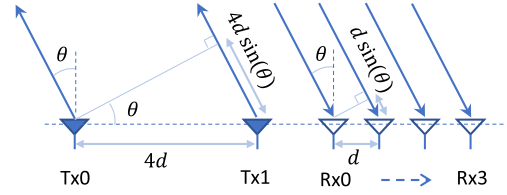

FIGURE 6. Angle estimation with linear transmitter and receiver antenna arrays.

The MIMO radar has multiple transmitter and multiple receiver antennas. As illustrated in Fig. 6, when four receiver antennas form a uniform linear array with the spacing d, the transmitter antennas are arranged on the same receiver array axis but with the spacing $4d$. Similar to the discussions in the previous section, at each of the receiver antennas, the reflected chirp signal from the transmitter antenna Tx1 travels an additional distance of $4d\sin(\theta)$ as compared to the signal from the antenna Tx0. The additional travel distance results in a phase shift of

$$\Delta f = 4Sd\sin(\theta)/c = N_R Sd\sin(\theta)/c, \qquad (46)$$
$$\Delta\phi = 8\pi d\sin(\theta)/\lambda = \omega_\theta N_R, \qquad (47)$$

in addition to that in (35), where ω_θ is defined (37) and N_R is the number of the receiver antennas. For the ease of presentation, define a row vector based on (39) for the 2-Tx-4-Rx TDM MIMO configuration (i.e., $N_T = 2$ and $N_R = 4$) as shown in Fig. 6, that is,

$$z_{k,l}^{(\iota)} = [z_{k,l}^{(\iota)}[0],\ z_{k,l}^{(\iota)}[1],\ \ldots,\ z_{k,l}^{(\iota)}[N_R - 1]], \qquad (48)$$

where

$$z_{k,l}^{(\iota)}[i] = Y_k^{(i,\iota)}[l] \qquad (49)$$

for $0 \leq k < N_s$, $0 \leq l < N_c$, $0 \leq i < N_R$, and $0 \leq \iota < N_T$. $Y_k^{(i,\iota)}[l]$ is the Doppler-DFT derived for the ith receiver antenna using the signal from the ιth transmitter antenna. Then, from (38) and (47), we can derive that

$$z_{k,l}^{(\iota)}[i] = X_0^{(0,0)}[k]P_{N_c}(\frac{2\pi}{N_c}l - \omega_v)e^{j(i+\iota N_R)\omega_\theta}, \qquad (50)$$

for $0 \leq k < N_s$, $0 \leq l < N_c$, $0 \leq i < N_R$, and $0 \leq \iota < N_T$, where $N_T = 2$, $N_R = 4$. $X_m^{(i,\iota)}[k]$ is the range-DFT of the mth chirp signal received at the ith receiver antenna from the ιth transmitter antenna.

We can observe from (50) that the Doppler-DFT data obtained using the signals from the two transmitter antennas can be concatenated together as the following,

$$z_{k,l} = [z_{k,l}^{(0)},\ z_{k,l}^{(1)},\ \ldots,\ z_{k,l}^{(N_T-1)}], \qquad (51)$$

where $z_{k,l}^{(\iota)}$ is the Doppler-DFT data obtained using the signal from the ιth transmitter antenna as defined in (48). Then, for the given values of k and l, $z_{k,l}$ in (51) is a discrete-time complex exponential signal of length $N_T \times N_R$ with the discrete-time angular frequency ω_θ defined in (37). Consequently, the concatenation strategy in (51) is equivalent to

using a radar configuration of one transmitter antenna and one linear receiver array of $N_T \times N_R$ antennas. In general, with a MIMO radar of N_T transmitter and N_R receiver antennas, we can synthesize a virtual uniform linear array of $N_T \times N_R$ receiver antennas. As can be seen from (43) and (44), the increased number of antennas in the virtual linear receiver array can effectively improve the angular resolution.

In practical implementation of MIMO radars, multiple transmitter antennas can operate in the time division multiplexing (TDM) mode as shown in Fig. 7 [12]. In the TDM mode, the transmitter antennas take turn to transmit the chirp signal. The time duration $T_a = T_c/N_T$ is the time taken by each transmitter antenna to transmit one chirp signal and T_c is the time for one round of transmission by all transmitter antennas. From (28), we can observe that improved angular resolution of the TDM MIMO radar is achieved at the cost of reduced maximum velocity that can be detected through Doppler processing.
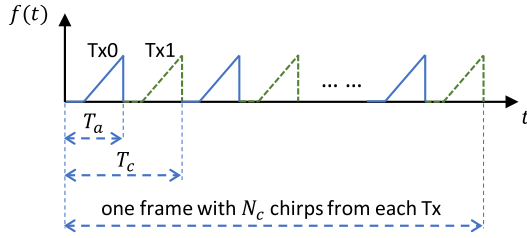

FIGURE 7. A frame of chirp signals with two TDM transmitter antennas.

The principle of MIMO radar can also be extended to multidimensional arrays. With a 2D MIMO array, it is possible to measure both azimuth and elevation angles of arrival, which is often necessary for automotive radar applications. Based on the derivations presented in this paper, extension to 2D TDM MIMO array is straightforward although quite tedious. Interested readers may find some useful details in [12].

B. COMPENSATION OF THE VELOCITY-INDUCED PHASE SHIFT

When the transmitter antennas of the MIMO radar operate in the TDM mode, as shown in Fig. 7, the chirp signals transmitted by two adjacent transmitter antennas are separated by T_a in time, while $T_a = T_c/N_T$ and N_T is the number of transmitter antennas. Similar to the discussions for the Doppler processing, if the velocity of the object is v, over the time duration of T_a, the object travels a distance of $\Delta r = vT_a$. Thus, the IF signal derived using the transmitter antenna Tx1 encounters additional shifts in frequency and phase, i.e.,

$$\Delta f = 2S\Delta r/c = 2SvT_a/c = 2SvT_c/(cN_T), \quad (52)$$

$$\Delta \phi = 4\pi \Delta r/\lambda = 4\pi vT_a/\lambda = \omega_v/N_T, \quad (53)$$

relative to the signal derived using the antenna Tx0, in addition to that in (47). In these equations, ω_v is defined in (25) and N_T is the number of transmitter antennas in the MIMO radar. Again, the velocity-induced frequency shift in (52)

is negligible as compared to the IF signal frequency. However, for proper angle estimation using the TDM MIMO radar, the velocity-induced phase shift given in (53) needs to be removed before applying the angle-DFT to the virtual receiver array data defined in (51). Specifically, with the velocity-induced phase shift, the Doppler-DFT data given in (50) now becomes

$$z_{k,l}^{(\iota)}[i] = X_0^{(0,0)}[k]P_{N_c}(\frac{2\pi}{N_c}l - \omega_v)e^{j(i+\iota N_R)\omega_\theta}e^{j\iota\omega_v/N_T} \quad (54)$$

for $0 \le k < N_s$, $0 \le l < N_c$, $0 \le i < N_R$, and $0 \le \iota < N_T$.

To compensate the velocity-induced phase shift between the signals derived using different transmitter antennas, we apply a phase correction to $z_{k,l}^{(\iota)}[i]$ in (54) as the following,

$$\tilde{z}_{k,l}^{(\iota)}[i] = z_{k,l}^{(\iota)}[i]e^{-j2\pi\iota l/(N_cN_T)}, \quad (55)$$

for $0 \le k < N_s$, $-N_c/2 \le l < N_c/2$, $0 \le i < N_R$, and $0 \le \iota < N_T$. Then, define

$$\tilde{z}_{k,l}^{(\iota)} = [\tilde{z}_{k,l}^{(\iota)}[0], \tilde{z}_{k,l}^{(\iota)}[1], \dots, \tilde{z}_{k,l}^{(\iota)}[N_R - 1]], \quad (56)$$

$$\tilde{z}_{k,l} = [\tilde{z}_{k,l}^{(0)}, \tilde{z}_{k,l}^{(1)}, \dots, \tilde{z}_{k,l}^{(N_T-1)}]. \quad (57)$$

From (55), we can observe that the velocity-induced phase shift is completely removed from the virtual receiver antenna array data defined (57) when $\omega_v = 2\pi l/N_c$. Thus, in practice, the range-DFT and Doppler-DFT are applied first to detect objects in the range-velocity domain. Then, the angle-DFT is applied across virtual receiver antennas at the specific range-velocity cells where objects are detected. An implication of such a processing flow is that angle estimation performance directly depends on that of velocity estimation.

VII. RADAR SIGNAL PROCESSING FLOW

As discussed in the previous sections, radar transmits a frame of N_c chirps and use N_R receivers (or, $N_R \times N_T$ virtual receivers in the TDM MIMO mode) to receive the reflected chirp signals. Each received chirp signal results in a discrete-time IF signal of N_s samples. The data generated from one frame of chirps are organized in a 3D data block as shown in Fig. 8, which is referred to as radar data cube.
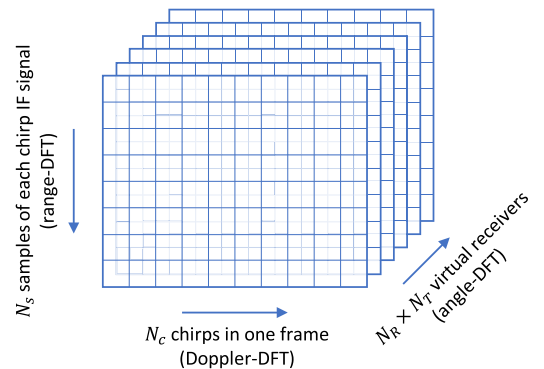

FIGURE 8. Illustration of the radar data cube and the 3D-DFT on the data.

The basic radar signal processing flow is shown in Fig. 9. Once the radar data cube is available, the range-DFT is first

applied to each of the sampled chirp IF signals (along the columns as shown in Fig. 8) for all chirps in the frame and for all virtual receivers. The Doppler-DFT is then applied along each of the rows across the N_c chirps to derive range-velocity spectrum for each of the virtual receivers. The constant false-alarm rate (CFAR) detector is typically applied to the range-velocity spectrum for object detection [5], [14]. The angle-DFT is then applied to each of the range-velocity cell containing the detected objects across all virtual receivers. FFT is almost always used for DFT. However, zoom-FFT and Chirp-Z transform can also be used when a portion of the spectrum needs to be analyzed with higher resolution [19].
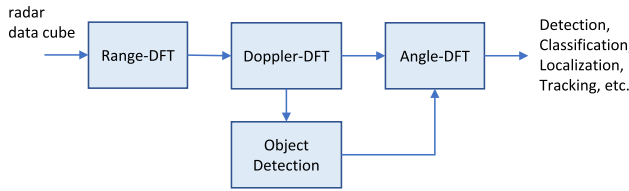

FIGURE 9. Block diagram of the radar signal processing flow.

VIII. SIMULATION RESULTS

To validate the analytical derivations presented in this paper, we have developed computer simulations in Python. In our implementation, NumPy is used for the FFT computation. The radar parameter values used in simulations are summarized in Table 1. The parameter values are determined to match the typical short-range radar requirements in the automotive application context [18]. The same parameter values are used in both simulations and experimental studies that are presented in this section and the next, respectively. In the results presented in this section, we have simulated five objects with various received signal amplitude (A), range (r), velocity (v), and angle (θ) configurations as listed in Table 2.

In simulations, the IF signal is first generated for each object by using the signal model in (8) and the frequency and phase shift models for the scenarios of multiple chirps, multiple receiver antennas, and the TDM MIMO radar configuration. The overall received IF signal is simply linear combination of the signals generated for each of the simulated objects.

The simulated IF signal is organized similar to the radar data cube structure shown in Fig. 8. Then, the range-DFT, Doppler-DFT, and angle-DFT are applied in sequence as described in this paper. FFT and Hanning window are used for all three DFTs. The linear and power spectra of range-DFT is shown in Fig. 10, following the definitions in [20]. The range power spectrum is averaged noncoherently over all chirps and virtual receivers. We can clearly observe spectrum spikes at the correct range coordinates corresponding to each of the simulated objects, which can be easily detected using the CFAR detector for object detection.

The range-velocity (i.e., range-Doppler) power spectrum is shown in Fig. 11 with a heatmap plot. From the figure,

TABLE 1. Radar parameter values used in simulations.

N_T	2	f_c	77 GHz
N_R	4	F_s	5 MHz
N_c	64	S	15.015 MHz/μs
N_s	250	T_c	$N_T \times 60.17\,\mu$s

TABLE 2. Object parameter values used in simulations.

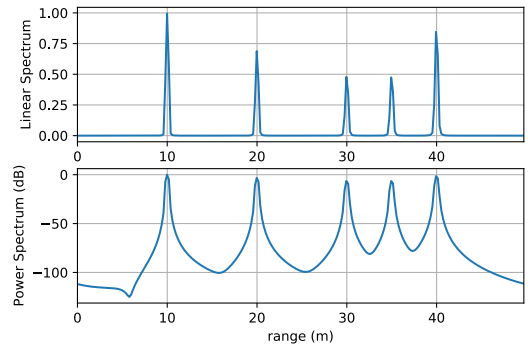|	A (V)	r (m)	v (m/s)	θ (degree)
1	1	10	0	0
2	0.7	20	-1.4	45
3	0.5	30	0.5	-15
4	0.5	35	0.2	-60
5	0.9	40	-1	-30

FIGURE 10. Linear and power spectra of the range-DFT in the range domain.

we can observe that the five simulated objects are clearly separated in the range-velocity domain. The range-velocity power spectrum is averaged noncoherently across all virtual receivers. Object detection algorithms can be easily applied to estimate the range and velocity of the objects.

The range-angle power spectrum is shown in Fig. 12 in the range-angle domain and in Fig. 13 in the 2D Cartesian spatial domain, both for the 2-Tx-4-Rx TDM MIMO configuration. For comparison, we have also included range-angle power spectrum for the 4-Tx-4-Rx TDM MIMO configuration in Fig. 14. To demonstrate the effectiveness of the compensation method for the velocity-induced phase shift as presented in Section VI-B, the range-angle power spectra derived with and without phase compensation are shown in Figs. 14a and 14b, respectively. We can observe the angle offsets of spectrum peaks as well as much higher spectrum side lobes when the velocity-induced phase shifts are not compensated.

With proper phase compensation, spectrum peaks provide accurate estimates of the object angles as shown in Figs. 12, 13, and 14a. However, it is important to note that the simulations do not include any noise or interference effects, and objects are well separated in the range-velocity domain. In practice, angle estimation accuracy is highly affected by noise and interference, and object resolving capability is
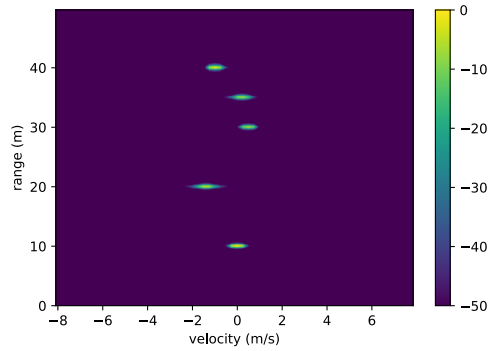
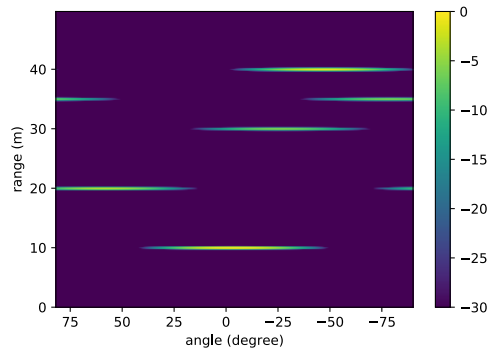**FIGURE 11.** Power spectrum of the Doppler-DFT in the range-velocity domain.

FIGURE 12. Power spectrum of the angle-DFT for the 2-Tx-4-Rx TDM MIMO configuration in the range-angle domain.
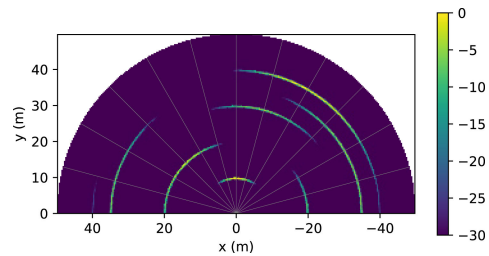

FIGURE 13. Power spectrum of the angle-DFT for the 2-Tx-4-Rx TDM MIMO configuration in the 2D spatial domain.

quite low in the angle domain for a small number of virtual receivers. Angular resolution improves as the number of virtual receivers increases as can be seen by comparing Figs. 13 and 14a. In addition, with a small number of virtual receivers, at wide angles (such as Object 4 with $-60°$ angle), we can clearly observe the aliasing of spectrum from negative angle to positive angle as a result of the periodicity of the DFT. Such aliasing in spectrum introduces further challenges in object detection and angle estimation.

IX. EXPERIMENTAL RESULTS

The experimental platform that we have used in this study is the AWR2243BOOST from Texas Instruments (TI), which is the second-generation 76 GHz to 81 GHz single-chip automotive mmWave radar sensor evaluation module. It can
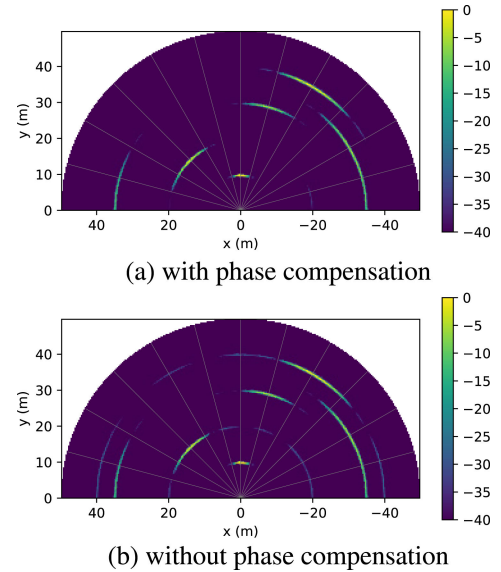

(a) with phase compensation

(b) without phase compensation

FIGURE 14. Power spectrum of the angle-DFT for the 4-Tx-4-Rx TDM MIMO configuration with and without compensation of the velocity-induced phase shift.

be configured to operate in the TDM MIMO mode with up to 3 transmitter antennas and 4 receiver antennas to estimate both azimuth and elevation angles [12], [18]. The FMCW chirp signal characteristics and the chirp frame structure are also configurable to meet the range and velocity estimation requirements of different application scenarios [18].

The experimental measurement system is used to collect data at the parking lot of the UNT Discovery Park as shown in Fig. 15. The radar system is configured using the same parameter values as the ones used in simulations shown in Table 1. The parameter values are determined to match the typical short-range radar requirements in the automotive application context [18]. The signal processing techniques presented in this paper have been implemented in Python and applied to the signals acquired using the AWR2243BOOST module. The raw radar data cube acquired using the AWR2243BOOST module is post-processed with the range-DFT, Doppler-DFT, and angle-DFT in sequence as illustrated in the block diagram in Fig. 9. The object detection step is omitted in processing in order to derive and visualize the power spectrum of the angle-DFT over the entire angular domain as shown in Fig. 16.

To demonstrate the effectiveness of the TDM MIMO configuration and the phase compensation method presented in this paper, we collected radar measurement data for a stationary car located at 10 m distance from the radar (i.e., the same scenario as shown in Fig. 15) using the 1-Tx-4-Rx and 2-Tx-4-Rx TDM MIMO configurations. The power spectra of the angle-DFT are presented in Fig. 16. From the results, we can clearly observe that the angular resolution of the 2-Tx-4-Rx configuration is much better than the 1-Tx-4-Rx configuration. With the 2-Tx-4-Rx TDM MIMO configuration, angular positions (i.e., AOA) of the car

FIGURE 15. Experimental study of the TDM MIMO FMCW mmWave radar using the TI AWR2243BOOST module.
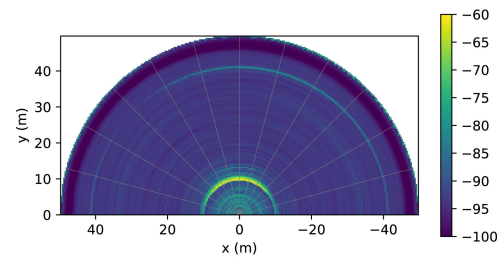
and the light pole at 40 m distance can be more accurately detected.

To validate the velocity estimation capability of the radar sensor, we introduced a person riding a bicycle to the measurement scenario shown in Fig. 15. Specifically, a car is parked stationary at 10 m distance right in front of the radar while a person riding a bicycle is situated on the right side of the car and the person/bicycle is at around 15 m distance from the radar. Fig. 17 shows the power spectrum of the Doppler-DFT of the data collected using the 2-Tx-4-Rx TDM MIMO configuration. The moving person/bicycle is observable from the power spectrum of the Doppler-DFT at around the coordinate (1.8 m/s, 15 m) in the range-velocity domain. In practice, the CFAR detector can be applied to the power spectrum as briefly discussed in Section VII. Then, the outputs of the object detection algorithm can be used for further application-specific processing for object detection, classification, localization, and tracking, etc.
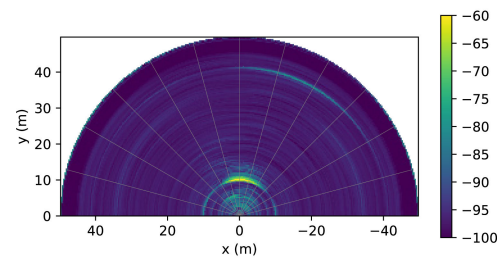
X. RELATED WORKS

Radar was initially developed for military applications, and it has a long history of research and development. To date, it has been successfully employed in a diverse range of applications. A number of radar-focused textbooks are available in the literature, including for example [14] and [15]. These textbooks contain comprehensive coverage on common terminologies, fundamental principles and processing algorithms, and various frameworks and taxonomy of many types of radar technologies and systems. However, such textbooks do not have detailed coverage on the latest developments of automotive radar technologies such as the TDM MIMO FMCW mmWave radar.

Reviews of the current state-of-the-art and future research directions of automotive radar technologies are available in more recent publications such as [5]–[7]. Different from our paper, such review papers focus more on the breadth of coverage, but not on the detailed derivations of any particular aspects of radar signal processing techniques. Brief tutorials focused on implementation details and practical aspects are now becoming available from the manufacturers of the

(a) with the 1-Tx-4-Rx configuration

(b) with the 2-Tx-4-Rx configuration

FIGURE 16. Power spectrum of the angle-DFT of a stationary car at 10 m distance measured using the 1-Tx-4-Rx and 2-Tx-4-Rx TDM MIMO configurations.
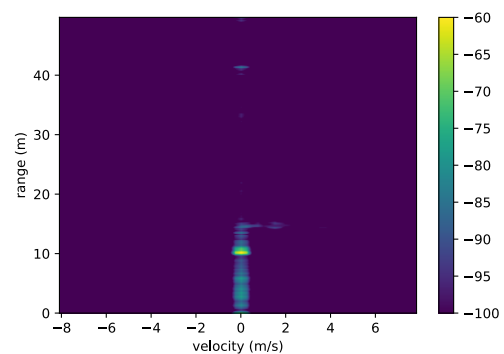

FIGURE 17. Power spectrum of the Doppler-DFT of a stationary car and a person riding a bicycle at around 15 m distance measured using the 2-Tx-4-Rx TDM MIMO configuration.

mmWave radar devices in the forms of whitepapers and application notes, including for example [12], [16]–[18]. Different from typical research papers from academia, such tutorials from industry often only contain limited introductory materials and selected results without sufficient analytical details or in-depth analysis. Thus, our paper well complements the existing tutorials in the literature.

Automotive radar technologies are currently under active research and development in both academia and industry. For related topics beyond the scope of this paper, interested readers may refer to [5]–[7], which have provided comprehensive reviews of the current research topics and future directions. The literature on automotive radars has been expanding dramatically in recent years. In addition to adapting classical radar technologies to automotive applications, there are also increasing interests in leveraging new advances in sensor fusion, machine learning, artificial

intelligence, and computer vision to address a wide range of design challenges in automotive radars. For example, some recent studies include MIMO techniques [6]–[11], antenna array configurations [21], [22], radar point cloud [27]–[32], radar-related sensor fusion [38]–[41], parameter estimation [26], angle estimation [23]–[25], and micro-Doppler-based machine learning [5], [33]–[37], among many others.

It is important to note that joint radar and communication design has attracted great attention from research community in recent years [48], [49]. Driven by various design and application requirements, there has been increasing demand for radar and communication systems to coexist by sharing the spectrum. Interested readers may refer to [49] for a comprehensive review of the state-of-the-art and future research directions in the areas of radar-communication coexistence and dual-functional radar-communication systems. In addition to automotive applications, mmWave radars have been actively studied for many other applications such as occupancy estimation and human activity recognition [37], [42]–[46]. Different types of sensors have already been applied to this application domain, including visual, infrared, acoustic, pressure, and wearable sensors [43], [47]. However, it is expected that radar could provide unique sensing capabilities to complement other types of sensors.

For experimental studies, there are a few mmWave radar devices available from TI, NXP and other companies [3], [4]. Implementations and reference materials for various radar signal processing algorithms are available from radar device manufacturers as well as the MATLAB Radar Toolbox [50] and the open-source OpenRadar Python package [51].

XI. SUMMARY AND CONCLUSION

This paper presents a systematic review of the fundamental operating principles and the DFT-based signal processing techniques for the state-of-the-art TDM MIMO FMCW mmWave radars. The 3D Fourier transform methods for range processing, Doppler processing, and angle processing are presented in details using a consistent analytical framework. We have also included detailed derivations and explanations of the resolution and unambiguous estimation limits for range, velocity, and angle. Implementation and processing techniques for the TDM MIMO radars have been presented in details, including compensation of the velocity-induced phase shift that is unique to the TDM MIMO radars. Both simulation and experimental results are presented to validate the analytical derivations and analysis. The effects of the number of virtual receivers and the phase compensation technique are demonstrated through various simulation and experimental results. We have also presented a brief review of the related works to help guide readers in further exploration of the latest automotive radar technologies.

REFERENCES

[1] H. H. Meinel, "Evolving automotive radar: From the very beginnings into the future," in *Proc. 8th Eur. Conf. Antennas Propag. (EuCAP)*, Apr. 2014, pp. 3107–3114.

[2] B. Su, "5G and mmWave test challenges of autonomous driving," Keysight Technol., Santa Rosa, CA, USA, White Paper, Jan. 2018.

[3] A. Benjamin, "Enabling the highest performance front-end radar to help bring vision zero into reality," Texas Instrum., Dallas, TX, USA, White Paper, Mar. 2020.

[4] NXP. (2021). *TEF810X 77 GHz Automotive Radar Transceiver*. Fact Sheet, NXP B.V. [Online]. Available: https://www.nxp.com

[5] I. Bilik, O. Longman, S. Villeval, and J. Tabrikian, "The rise of radar for autonomous vehicles," *IEEE Signal Process. Mag.*, vol. 36, no. 5, pp. 20–31, Sep. 2019.

[6] S. M. Patole, M. Torlak, D. Wang, and M. Ali, "Automotive radars: A review of signal processing techniques," *IEEE Signal Process. Mag.*, vol. 34, no. 2, pp. 22–35, Mar. 2017.

[7] G. Hakobyan and B. Yang, "High-performance automotive radar," *IEEE Signal Process. Mag.*, vol. 36, no. 5, pp. 32–44, Sep. 2019.

[8] S. Lutz, K. Baur, and T. Walter, "77 GHz lens-based multistatic MIMO radar with colocated antennas for automotive applications," in *IEEE MTT-S Int. Microw. Symp. Dig.*, Jun. 2012, pp. 1–3.

[9] J. Li and P. Stoica, "MIMO radar with colocated antennas," *IEEE Signal Process. Mag.*, vol. 24, no. 5, pp. 106–114, Sep. 2007.

[10] D. Cohen, D. Cohen, and Y. C. Eldar, "High resolution FDMA MIMO radar," *IEEE Trans. Aerosp. Electron. Syst.*, vol. 56, no. 4, pp. 2806–2822, Aug. 2020.

[11] K. Rambach and B. Yang, "MIMO radar: Time division multiplexing vs. code division multiplexing," in *Proc. Int. Conf. Radar Syst. (Radar)*, Oct. 2017, pp. 1–5.

[12] S. Rao, "MIMO radar," Texas Instrum., Dallas, TX, USA, Appl. Rep. SWRA554A, Jul. 2018.

[13] S. Samala, "Signal processing and frequency generation in FMCW RADAR," in *Proc. IEEE Custom Integr. Circuits Conf. (CICC)*, Apr. 2018, pp. 1–73.

[14] B. R. Mahafza, *Radar Systems Analysis and Design using MATLAB*, 3rd ed. Boca Raton, FL, USA: CRC Press, 2013.

[15] M. A. Richards, *Fundamentals of Radar Signal Processing*, 2nd ed. New York, NY, USA: McGraw-Hill, 2014.

[16] C. Iovescu and S. Rao, "The fundamentals of millimeter wave sensors," Texas Instrum., Dallas, TX, USA, White Paper SPYY005A, Jul. 2016.

[17] K. Ramasubramanian, "Using a complex-baseband architecture in FMCW radar systems," Texas Instrum., Dallas, TX, USA, White Paper SPYY007, May 2017.

[18] V. Dham, "Programming chirp parameters in TI radar devices," Texas Instrum., Dallas, TX, USA, Appl. Rep. SWRA553A, Feb. 2020.

[19] J. G. Proakis and D. G. Manolakis, *Digital Signal Processing*, 4th ed. Upper Saddle River, NJ, USA: Pearson, 2007.

[20] G. Heinzel, A. Rüdiger, and R. Schilling. (2002). *Spectrum and Spectral Density Estimation by the Discrete Fourier Transform (DFT)*. MPG.PuRe. [Online]. Available: https://hdl.handle.net/11858/00-001M-0000-0013-557A-5

[21] E. BouDaher, F. Ahmad, and M. G. Amin, "Sparsity-based direction finding of coherent and uncorrelated targets using active nonuniform arrays," *IEEE Signal Process. Lett.*, vol. 22, no. 10, pp. 1628–1632, Oct. 2015.

[22] A. H. Shaikh, X. Dang, T. Ahmed, and D. Huang, "New transmit-receive array configurations for the MIMO radar with enhanced degrees of freedom," *IEEE Commun. Lett.*, vol. 24, no. 7, pp. 1534–1538, Jul. 2020.

[23] L. R. Cenkeramaddi, P. K. Rai, A. Dayal, J. Bhatia, A. Pandya, J. Soumya, A. Kumar, and A. Jha, "A novel angle estimation for mmWave FMCW radars using machine learning," *IEEE Sensors J.*, vol. 21, no. 8, pp. 9833–9843, Apr. 2021.

[24] H. Wang, X. Wang, M. Huang, L. Wan, and T. Su, "RxCV-based unitary SBL algorithm for off-grid DOA estimation with MIMO radar in unknown non-uniform noise," *Digit. Signal Process.*, vol. 116, Sep. 2021, Art. no. 103119.

[25] L. Wan, K. Liu, Y.-C. Liang, and T. Zhu, "DOA and polarization estimation for non-circular signals in 3-D millimeter wave polarized massive MIMO systems," *IEEE Trans. Wireless Commun.*, vol. 20, no. 5, pp. 3152–3167, May 2021.

[26] Y.-C. Lin, T.-S. Lee, Y.-H. Pan, and K.-H. Lin, "Low-complexity high-resolution parameter estimation for automotive MIMO radars," *IEEE Access*, vol. 8, pp. 16127–16138, 2020.

[27] Z. Zhao, Y. Song, F. Cui, J. Zhu, C. Song, Z. Xu, and K. Ding, "Point cloud features-based kernel SVM for human-vehicle classification in millimeter wave radar," *IEEE Access*, vol. 8, pp. 26012–26021, 2020.

[28] A. Danzer, T. Griebel, M. Bach, and K. Dietmayer, "2D car detection in radar data with PointNets," in *Proc. IEEE Intell. Transp. Syst. Conf. (ITSC)*, Oct. 2019, pp. 61–66.

[29] F. Jin, A. Sengupta, S. Cao, and Y.-J. Wu, "mmWave radar point cloud segmentation using GMM in multimodal traffic monitoring," in *Proc. IEEE Int. Radar Conf.*, Apr. 2020, pp. 732–737.

[30] Q. Zheng, Y. Xie, L. Yang, J. Li, C. Song, Z. Xu, and K. Ding, "An improved scheme for high-resolution point cloud map generation based on FMCW radar," in *Proc. IEEE 11th Sensor Array Multichannel Signal Process. Workshop (SAM)*, Jun. 2020, pp. 1–5.

[31] O. Schumann, J. Lombacher, M. Hahn, C. Wohler, and J. Dickmann, "Scene understanding with automotive radar," *IEEE Trans. Intell. Vehicles*, vol. 5, no. 2, pp. 188–203, Jun. 2020.

[32] A. Ngo, M. P. Bauer, and M. Resch, "Deep evaluation metric: Learning to evaluate simulated radar point clouds for virtual testing of autonomous driving," in *Proc. IEEE Radar Conf. (RadarConf)*, May 2021, pp. 1–6.

[33] V. C. Chen, F. Li, S.-S. Ho, and H. Wechsler, "Micro-Doppler effect in radar: Phenomenon, model, and simulation study," *IEEE Trans. Aerosp. Electron. Syst.*, vol. 42, no. 1, pp. 2–21, Jan. 2006.

[34] Y. Ding and J. Tang, "Micro-Doppler trajectory estimation of pedestrians using a continuous-wave radar," *IEEE Trans. Geosci. Remote Sens.*, vol. 52, no. 9, pp. 5807–5819, Sep. 2014.

[35] V. Chen, *The Micro-Doppler Effect Radar*. Norwood, MA, USA: Artech House, 2019.

[36] M. Ostovan, S. Samadi, and A. Kazemi, "DecompNet: Deep context dependent decomposition network for micro-Doppler signature of walking human," *IEEE Sensors J.*, vol. 21, no. 22, pp. 25862–25869, Nov. 2021.

[37] H. T. Le, S. L. Phung, and A. Bouzerdoum, "A fast and compact deep Gabor network for micro-Doppler signal processing and human motion classification," *IEEE Sensors J.*, vol. 21, no. 20, pp. 23085–23097, Oct. 2021.

[38] H.-K. Lee, S.-G. Shin, and D.-S. Kwon, "Design of emergency braking algorithm for pedestrian protection based on multi-sensor fusion," *Int. J. Automot. Technol.*, vol. 18, no. 6, pp. 1067–1076, Aug. 2017.

[39] N. S. Zewge, Y. Kim, J. Kim, and J.-H. Kim, "Millimeter-wave radar and RGB-D camera sensor fusion for real-time people detection and tracking," in *Proc. Int. Conf. Robot Intell. Technol. Appl.*, Nov. 2019, pp. 93–98.

[40] A. Klautau, N. Gonzalez-Prelcic, and R. W. Heath, "LIDAR data for deep learning-based mmWave beam-selection," *IEEE Wireless Commun. Lett.*, vol. 8, no. 3, pp. 909–912, Jun. 2019.

[41] R. Zhang and S. Cao, "Extending reliability of mmWave radar tracking and detection via fusion with camera," *IEEE Access*, vol. 7, pp. 137065–137079, 2019.

[42] J. L. Kernec, F. Fioranelli, C. Ding, H. Zhao, L. Sun, H. Hong, J. Lorandel, and O. Romain, "Radar signal processing for sensing in assisted living," *IEEE Signal Process. Mag.*, vol. 36, no. 4, pp. 29–41, Jul. 2019.

[43] S. Z. Gurbuz and M. G. Amin, "Radar-based human-motion recognition with deep learning," *IEEE Signal Process. Mag.*, Jul. 2019.

[44] H. Cui and N. Dahnoun, "High precision human detection and tracking using millimeter-wave radars," *IEEE Aerosp. Electron. Syst. Mag.*, vol. 36, no. 1, pp. 22–32, Jan. 2021.

[45] Y. Kim, S. Choudhury, and H.-J. Kong, "Application of micro-Doppler signatures for estimation of total energy expenditure in humans for walking/running activities," *IEEE Access*, vol. 4, pp. 1560–1569, 2016.

[46] A. Sengupta, F. Jin, and S. Cao, "NLP based skeletal pose estimation using mmWave radar point-cloud: A simulation approach," in *Proc. IEEE Radar Conf. (RadarConf)*, Sep. 2020, pp. 1–6.

[47] V. Chidurala and X. Li, "Occupancy estimation using thermal imaging sensors and machine learning algorithms," *IEEE Sensors J.*, vol. 21, no. 6, pp. 8627–8638, Mar. 2021.

[48] S. H. Dokhanchi, B. S. Mysore, K. V. Mishra, and B. Ottersten, "A mmWave automotive joint radar-communications system," *IEEE Trans. Aerosp. Electron. Syst.*, vol. 55, no. 3, pp. 1241–1260, Jun. 2019.

[49] F. Liu, C. Masouros, A. P. Petropulu, H. Griffiths, and L. Hanzo, "Joint radar and communication design: Applications, state-of-the-art, and the road ahead," *IEEE Trans. Commun.*, vol. 68, no. 6, pp. 3834–3862, Jun. 2020.

[50] *MATLAB Radar Toolbox*. MathWorks. (2021). [Online]. Available: https://www.mathworks.com/help/radar

[51] E. Pan, J. Tang, D. Kosaka, R. Yao, and A. Gupta. *OpenRadar*. GitHub Repository. [Online]. Available: https://github.com/presenseradar/openradar
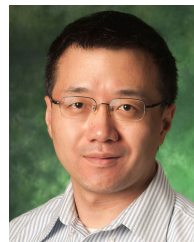
XINRONG LI (Senior Member, IEEE) received the B.E. degree in electrical engineering from the University of Science and Technology of China (USTC), Hefei, China, in 1995, the M.E. degree in electrical engineering from the National University of Singapore (NUS), in 1999, and the Ph.D. degree in electrical engineering from the Worcester Polytechnic Institute (WPI), Worcester, MA, USA, in 2003. From 2003 to 2004, he was a Postdoctoral Research Fellow at the Center for Wireless Information Network Studies, Worcester Polytechnic Institute. He has been working with the Department of Electrical Engineering, University of North Texas, Denton, TX, USA, as an Assistant Professor, since 2004, and an Associate Professor, since 2010. His research interests include signal processing, machine learning, sensor systems, and wireless networks.

XIAODONG WANG received the B.E. degree from the Shandong University of Science and Technology, Qingdao, China, in 2017. She is currently pursuing the Ph.D. degree with the Department of Electrical Engineering, University of North Texas (UNT), Denton, TX, USA. In the past few years, she has been working as a Teaching Assistant and a Research Assistant at the Embedded Sensing and Processing Systems (ESPS) Laboratory, UNT. Her research interests include signal processing, embedded systems, and machine learning.

QING YANG (Senior Member, IEEE) received the Ph.D. degree in computer science and software engineering from Auburn University, Auburn, AL, USA, in 2011. He is currently an Assistant Professor with the Department of Computer Science and Engineering, University of North Texas, Denton, TX, USA. His research is funded by the U.S. National Science Foundation, the U.S. Federal Highway Administration, the Office of Naval Research, Toyota InfoTech Inc., Fujitsu Laboratories of America Inc., and the University of North Texas Office of the Vice President for Research and Innovation. His current research interests include connected and autonomous vehicles, the Internet of Things, network security, and privacy.

SONG FU (Senior Member, IEEE) received the B.S. degree in computer science from the Nanjing University of Aeronautics and Astronautics, China, in 1999, the M.S. degree in computer science from Nanjing University, China, in 2002, and the Ph.D. degree in computer engineering from Wayne State University, in 2008. He is currently a Professor of computer science and engineering with the University of North Texas, Denton, TX, USA. His research has been sponsored by NSF, DOE, DOD, Toyota, Fujitsu, Google, Amazon, Cisco, Nvidia, and Xilinx. His research interests include parallel and distributed systems, machine learning, cloud and edge computing, connected and autonomous vehicles, system reliability, and high-performance computing. He is a member of ACM. He directs the Dependable Computing Systems Laboratory. He also serves as the Associate Chair for research and outreach.

• • •